RSC Advances

PAPER

View Article Online
View Journal | View Issue

Check for updates

Cite this: *RSC Adv.*, 2020, **10**, 2472

MnO_x dispersed on attapulgite derived Al-SBA-15: a promising catalyst for volatile organic compound combustion†

Jie Meng, Fan Fang, Nengjie Feng, Hui Wan* and Guofeng Guan*

Received 8th October 2019
Accepted 13th December 2019

DOI: 10.1039/c9ra08157g

rsc.li/rsc-advances

To improve the catalytic activity when utilizing metal oxides for the combustion of VOCs, Mn/Al-SBA-15 catalysts have been successfully synthesized through an emerging wetness impregnation technique involving $Mn(NO_3)_2$ on Al-SBA-15, which has been directly prepared from attapulgite by a hydrothermal method. Compared to Mn/SBA-15, which is prepared with TEOS as its silicon source, all the as-prepared Mn/Al-SBA-15 catalysts demonstrated enhanced catalytic performance in the oxidation of toluene. From this research, the 8% Mn/Al-SBA-15 catalyst presented the best catalytic performance, due to the high efficiency resulting from the high chemical valence of Mn^{4+}. When the concentration of toluene was 2000 ppm, and the space velocity was 60 000 mL $(g\ h)^{-1}$, 8% Mn/Al-SBA-15 could effectively reduce the T_{50} and T_{90} values of toluene to 201 and 278 °C, respectively; while the 8% Mn/SBA-15 catalyst could reduce the T_{50} and T_{90} values of toluene to 223 and 298 °C, respectively. A systematic investigation has been conducted to reveal the synergistic effects of Al doping and manganese loading on the enhanced catalytic performance. The experiments showed impressive results, demonstrating that Al doping can not only increase the surface acidity of SBA-15, but it can also be beneficial for achieving a uniform dispersion of MnO_x on the surface and in the pores of Al-SBA-15, resulting in the enhancement of the catalytic performance.

1. Introduction

Volatile organic compounds (VOCs) emitted from industry, transport and residential/service sectors are considered to be a major source of air pollutants.[1–3] Offensive odors, toxic gases, the formation of ground-level ozone and chemical smog resulting from petrochemicals, which are all part of environmental problems, are associated with the emissions of VOCs.[4–6] In addition, VOCs are harmful to human health even in very low concentrations.[5–7] Hence, strict legislations have been established to reduce and even eradicate the impact of VOC emissions, in order to protect both the environment and human health.[7] To meet these requirements, many techniques for VOC removal have been developed, such as adsorption, membrane separation, condensation, *etc.*[8,9] Among them, the catalytic combustion of VOCs has been widely regarded as the most economical and promising method due to the lower reaction temperature and better performance in diluting pollutants with a concentration of less than 1%.

Up to now, the catalysts for catalytic combustion mainly focused on the utilization of noble metal-based catalysts (such as Pd, Pt, *etc.*)[10,11] to transmit metal oxide-based catalysts (such as Co_3O_4, CeO_2, *etc.*).[12–14] Although noble metals usually possess higher activities than non-noble metal oxides, especially at relatively lower temperatures, their higher manufacturing costs, sensitivity to poisoning and lower thermal stability are reasons for their limited applications in the chemical industry.[15] In contrast, transition metal oxide-based catalysts exhibit a lot of technical and commercial superiorities (lower cost, better resistance against poisons, *etc.*) that make them ideal candidates over noble metals in practical applications.[16,17] Therefore, manganese oxides (MnO_x) have been considered as one of the best materials for the catalytic combustion of VOCs in light of their low toxicity, excellent redox properties and their strong oxygen storage/release ability.[18–23] However, despite these practical advantages, there is still a huge gap between the activity of MnO_x and noble metal catalysts. To reduce the gap, researchers have previously deposited MnO_x on supports (*e.g.* Al_2O_3, SiO_2 and TiO_2) to achieve high dispersion of the active sites and enhancement of the catalytic activity.[24–27] During this procedure, the nature and property of the support material significantly affects the catalytic performance due to the strong metal-support interaction.[28,29]

State Key Laboratory of Materials-Oriented Chemical Engineering, College of Chemical Engineering, Jiangsu National Synergetic Innovation Center for AdvancedMaterials, Jiangsu Collaborative Innovation Center for Advanced Inorganic FunctionComposites, Nanjing Tech University, Nanjing 210009, P. R. China. E-mail: guangf@njtech.edu.cn; wanhui@njtech.edu.cn; Tel: +86 25 83587198

† Electronic supplementary information (ESI) available. See DOI: 10.1039/c9ra08157g

Open Access Article. Published on 14 January 2020. Downloaded on 4/16/2026 1:09:03 PM.
This article is licensed under a Creative Commons Attribution-NonCommercial 3.0 Unported Licence.

This journal is © The Royal Society of Chemistry 2020

Open Access Article. Published on 14 January 2020. Downloaded on 4/16/2026 1:09:03 PM.
This article is licensed under a Creative Commons Attribution-NonCommercial 3.0 Unported Licence.

Mesoporous SBA-15 has been widely considered as one of the most suitable support materials in the catalytic combustion of VOCs,[30–33] and is dependent on its super high surface area, adjustable pore size from 3 to 30 nm, its ordered pore structure, and its high thermal and hydrothermal stability. However, due to the lack of active sites in the structure, SBA-15 hardly makes a direct contribution to the catalytic activity except for the stabilization and dispersion of the active components.[34–39] In order to further improve its catalytic combustion performance, atom (*e.g.* Al, Fe and Co) doping has been generally adopted to create acidic and defect sites in the mesoporous SBA-15, which can not only generate electron-rich oxygen vacancies but also enhance the dispersion and stability of the supported active metal or metal oxide species.[36] For example, Li *et al.* reported that the integration of Fe in SBA-15 can accelerate the generation of a hydroxy radical during the catalytic ozonation of oxalic acid, leading to significant improvements in the catalytic activity of SBA-15.[37] Cui *et al.* exploited Ag/Al-SBA-15 by an *in situ* "pH-adjusting" method and a subsequent impregnation method. The catalytic results indicated that the doping of a small amount of Al was beneficial to the formation of small-sized Ag particles and the high dispersion in the channel, leading to the improvement in the catalytic activity.[38]

Inspired by these results, in order to optimize the catalytic performances of MnO_x and atom doping, we proposed the transformation of the Mn/Al-SBA-15 catalyst to achieve high activity in the catalytic combustion of VOCs. Al-SBA-15 was directly prepared from attapulgite by hydrothermal and calcination methods. Following this, $Mn(NO_3)_2$, which was prepared as a precursor of the active species, was deposited into Al-SBA-15 through an emerging wetness impregnation method. The catalytic activities of the as-prepared Mn/Al-SBA-15 composites were evaluated in toluene oxidation and methyl acetate oxidation reactions. In addition, we carried out a systematic investigation into the effects of Al *in situ* doping and the loading amounts of Mn species on the structure and catalytic oxidation performance of Mn/Al-SBA-15.

2. Experimental

2.1 Materials

Attapulgite was obtained from Xuyi, China, and had the following chemical composition (wt%):[29,40,41] SiO_2, 54.30; MgO, 12.71; Al_2O_3, 7.92; Fe_2O_3, 4.71; CaO, 3.42; K_2O, 0.62; MnO_x, 0.32; H_2O, 16.00. Poly(ethylene oxide) poly(propylene oxide) poly(ethylene oxide) (P123, $EO_{20}PO_{70}EO_{20}$), methyl acetate (98%, AR), tetraethyl orthosilicate (TEOS 98%, AR) and ethyl alcohol (95%, AR) were purchased from Aladdin Industrial Inc. Sodium hydroxide (NaOH, AR), hydrochloric acid (HCl, 37%), $Mn(NO_3)_2$ solution (50 wt%, AR) and toluene (99.5%, AR) were purchased from Sinopharm Chemical Reagent Co. Ltd. All of the reagents were of analytical grade and were used without any further purification.

2.2 Catalyst preparation

Attapulgite clay was pretreated *via* acid treatment, ball milling, and alkali fusion. The resulting powders were subsequently poured into a ball mill for grinding at a speed of 400 rpm for 2 h. The obtained solid (10 g) was treated with 15 g of NaOH at 600 °C for 5 h. After cooling down to room temperature, the resulting solid was dissolved in 400 mL of deionized water and stirred for 4 h before another 12 h of standing time at room temperature. The leaching liquid (supernatant) was used as Si and Al sources.[42]

The Al-SBA-15 support was synthesized following the procedure described by Zhao *et al.* with some modifications.[43] 4 g of P123 was dissolved into 122 mL of HCl (2 M) solution, and this was subsequently stirred at 38 °C for 1 h and named as solution A. Then, a certain amount of purified attapulgite clay was added dropwise into solution A and the pH value of solution A was adjusted to pH = −0.4 with dropwise addition of concentrated HCl under constant magnetic stirring at 40 °C for 20 h, and this was called solution B. Subsequently, solution B was transferred into a 200 mL Teflon-lined stainless autoclave and heated at 100 °C for 24 h. Upon leaving solution B to cool to room temperature, the solid precipitates were separated by filtration, washed with deionized water and ethanol several times, and then dried at 80 °C. Afterwards, the solid precipitates were dried by calcination at 550 °C for 5 h with a ramping rate of 2 °C min^{-1}. After cooling to room temperature, white powders were obtained.

The Mn/Al-SBA-15 catalyst was prepared by a conventional incipient wetness impregnation method. The Al-SBA-15 support was immersed in a $Mn(NO_3)_2$ aqueous solution (Mn weight loading of 2%, 4%, 6%, 8%, and 10%) after being stirred for 3 h at room temperature. Subsequently, the temperature was increased to 100 °C for complete water evaporation, followed by milling and annealing at 550 °C under an air atmosphere for 5 h at a ramping rate of 2 °C min^{-1}. After cooling to room temperature, the products were obtained. A detailed schematic illustration of the synthesis of Mn/Al-SBA-15 could be identified during the preparation process and is described in Scheme 1.

2.3 Characterization

The X-ray diffraction (XRD) patterns were recorded on a Bruker D8 advance spectrometer with Cu Kα radiation ($\lambda = 0.154$ nm), operated at 40 mA and 40 kV. Thermogravimetric (TG) analysis of the samples was carried out on a synchronous thermal analyzer model STA449, and the tests were carried out under an air atmosphere at a heating rate of 10 °C min^{-1}. The contents of the elements and oxides in the attapulgite were measured using a ZSX Primus II X-ray fluorescence (XRF) spectrometer from Rigaku, Japan. Fourier transform infrared (FT-IR) spectroscopy from 400–2000 cm^{-1} was acquired using a Thermo Nicolet 870 spectrophotometer using anhydrous KBr as a dispersing agent. Transmission electron microscope (TEM) images were obtained on a JOEL JEM 2010 transmission electron microscope. The samples were supported on carbon-coated copper grids for the experiment. The specific surface areas (SBET) were obtained from N_2 adsorption–desorption isotherms at 77 K (ASAP 2010, Micromeritics USA) on the samples preheated at 120 °C for 12 h in a vacuum. The S_{BET}

Open Access Article. Published on 14 January 2020. Downloaded on 4/16/2026 1:09:03 PM.
This article is licensed under a Creative Commons Attribution-NonCommercial 3.0 Unported Licence.

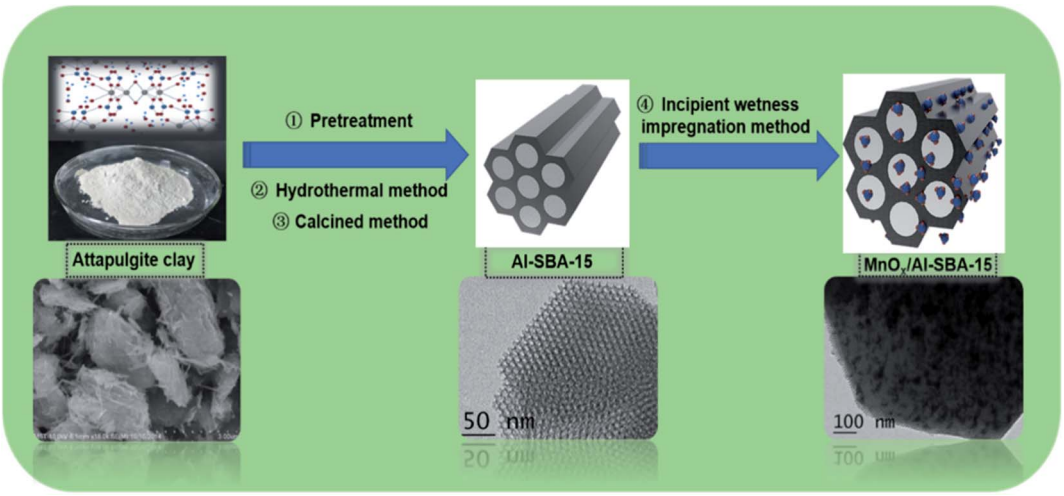

Scheme 1 A schematic illustration of the synthesis of Mn/Al-SBA-15.

values were calculated using the Brunauer Emmett Teller (BET) method. Temperature-programmed reduction with hydrogen (H_2-TPR) was carried out using a purified mixture of N_2/H_2 (90/10 vol%, air liquid) serving as a simultaneous carrier and reducing gas at a total flow rate of 40 mL min^{-1}. Before the measurements, a catalyst sample (40 mg) was preheated in a dry He stream at 350 °C for 30 min. Afterwards, the sample was cooled down to room temperature and the TPR experiment was initialized. The sample was heated at a rate of 10 °C min^{-1} to a final temperature of 900 °C. The H_2 consumption was measured at a final temperature of 900 °C. The H_2 consumption was measured by a thermal conductivity detector against NiO (99.999%, Aldrich) used for calibration of H_2 consumption. The XAS measurements for the Mn K-edge were performed in the transmission mode on beam line 20-BMB with an electron energy of 7 GeV and an average current of 100 mA, located in the Advanced Photon Source at the Argonne National Laboratory. The radiation was monochromatized by a Si (111) double-crystal monochromator. XANES and EXAFS data reduction and analysis were processed by Athena software.

2.4 Evaluation of catalytic performance

The catalysts were tested for the total oxidation of toluene on a fixed-bed reactor. 100 mg of the catalyst was comminuted and sieved to a particle size of a 40–60 mesh that was diluted with 300 mg of quartz sands. The mixture was placed in a central position of the quartz flow microreactor on a quartz wool plug and was outgassed prior to a catalytic run at 500 °C for 30 min in flowing air (60 000 mL (g h)$^{-1}$). Subsequently, toluene (2000 ppm), which was diluted with air, passed through the catalyst bed at a total flow rate of 200 mL min^{-1} after the reactor was cooled down to 100 °C, and the catalytic tests were carried out at a rate of 2 °C min^{-1} in the reactor until the temperature was heated to 400 °C. The reactor was maintained for 45 min with three 15 min lasting analyses of the organic products separated with a SE-30 column using a gas chromatograph (SP-6890) equipped with an FID. Each catalytic test was repeated three times in order to check the reproducibility.

3. Results and discussion

3.1 Catalyst characterization

The chemical composition of attapulgite was analyzed by thermogravimetric (TG) and X-ray fluorescence (XRF) analyses, as presented in Fig. S1 and Table S1.† It can be clearly seen from Fig. S1† that attapulgite has four distinct weight loss sections. Below 100 °C, the adsorbed water was removed and the weight loss was about 5%. In the range from 100 °C to 200 °C, the water in the pores was removed and the weight loss was about 5%. Between 300 °C and 500 °C, the weight loss was about 4%, and this could be attributed to the removal of crystal water. In addition, the weight loss between 500 °C and 700 °C was about 2%, where the structural water was removed. Table S1† shows that the molar ratio of the silicon element to other metal elements in attapulgite was close to that of the theoretical value (8 : 5), indicating that the quality of the attapulgite used was higher. It can also be seen from Table S1† that only 0.04 wt% MnO_x, 0.05 wt% K_2O and 0.09 wt% Fe_2O_3 were left after treatment. These amounts are small, and it was determined that 0.08 wt% MgO and 0.02 wt% CaO are also left. These results prove that a small amount of Mn, K, Fe and other elements have been left after the attapulgite original soil was treated by pulverization, washing, *etc.*, while they could be removed by the pickling step, and this was an ideal raw material for the preparation of silica-aluminum ordered mesoporous molecular sieves.

The structural properties and compositions of the as-prepared Mn/SBA-15 and Mn/Al-SBA-15 samples were investigated by X-ray diffraction (XRD). From the small-angle diffraction patterns (Fig. 1a), it could be clearly seen that Al-SBA-15 exhibited three well-resolved peaks at $2\theta = 0.8$, 1.6 and 1.8°, indexed to the (100), (110) and (200) reflections of a *P6mm* hexagonal symmetry, which is very consistent with the results of pristine SBA-15, reported before.[44] Moreover, the peak intensity

 This journal is © The Royal Society of Chemistry 2020

Open Access Article. Published on 14 January 2020. Downloaded on 4/16/2026 1:09:03 PM.
This article is licensed under a Creative Commons Attribution-NonCommercial 3.0 Unported Licence.

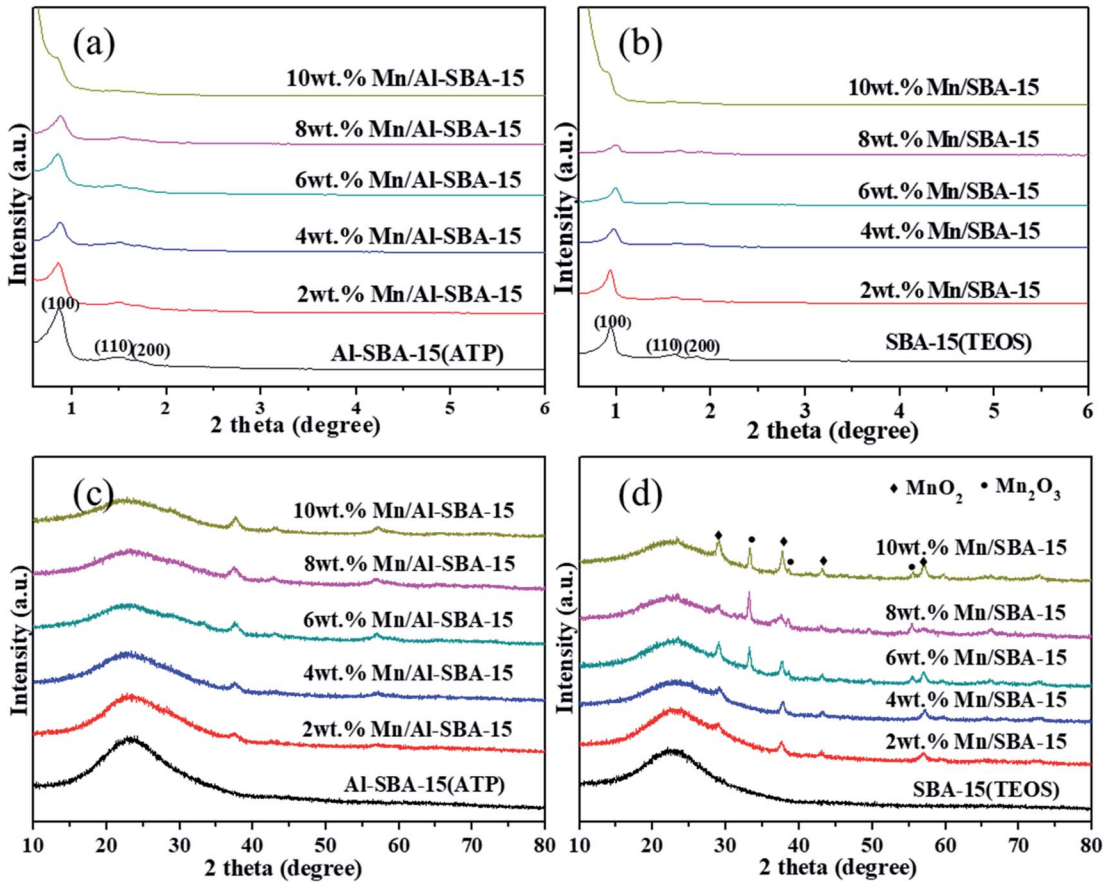

Fig. 1 Small-angle (a and b) and wide-angle (c and d) XRD patterns of the as-prepared catalysts.

decreased as the loading amount of MnOx in Al-SBA-15 increased, while the three peak positions remained unchanged. This phenomenon can be ascribed to the integration of a small amount of Mn species into the channels of SBA-15, which reduced the long-range order of the hexagonally arranged porosity in SBA-15.[45] Fig. 1c exhibits the wide-angle XRD patterns of the Al-SBA-15 and Mn/Al-SBA-15 catalysts. It can clearly be seen that the one broad peak from 20° to 25° is ascribed to amorphous silica. Remarkably, with the addition of the Mn species, several distinct diffraction peaks appeared and could not be simply assigned to one type of manganese oxide. The peaks at $2\theta = 37.3$, 42.9, and 56.6° could be attributed to the presence of α-MnO_2 (JCPDS PDF 44-0141). Moreover, peaks with 2θ at 33.1° and 38.2° corresponded to Mn_2O_3 (JCPSD PDF 71-0636). Interestingly, the peak intensities of the manganese species belonging to the Mn/Al-SBA-15 catalyst were significantly lower than those of Mn/SBA-15 with the same loading of Mn, and this may be as a result of the higher dispersion of Mn on Al-SBA-15.[46,47]

The chemical structure of the samples was further analyzed by FT-IR spectroscopy, as presented in Fig. 2 and S2.† Fig. S2† shows the FT-IR spectrum of the attapulgite and the attapulgite after acidification with 6 mol L^{-1} hydrochloric acid. For attapulgite, the wave numbers, which ranged from 3700 to 3200 cm^{-1} revealed the vibration peak of the hydroxyl OH, indicating that the surface of the attapulgite was rich in a large number of hydroxyl groups. The vibration peak at 3617 cm^{-1} was attributed to the Al–OH vibration in the attapulgite, indicating that Al occupied the coordination center of most octahedrons. The peak near 1030 cm^{-1} was an asymmetric stretching vibration peak of the Si–O bond, while the symmetry

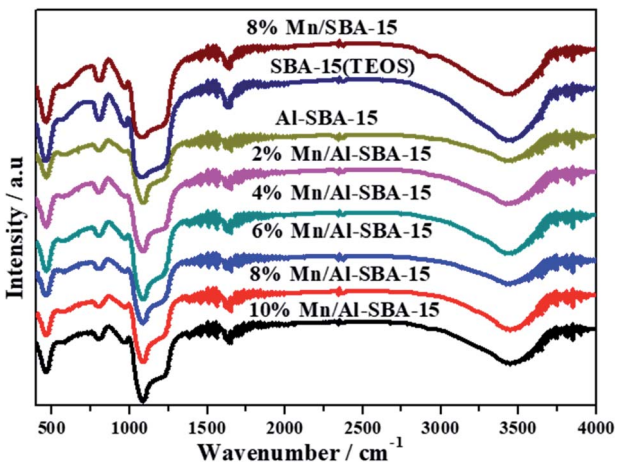

Fig. 2 FT-IR patterns of the as-prepared catalysts.

Open Access Article. Published on 14 January 2020. Downloaded on 4/16/2026 1:09:03 PM.
This article is licensed under a Creative Commons Attribution-NonCommercial 3.0 Unported Licence.

stretching vibration peak near the 790 cm^{-1} was from the Si–O–Si bond. The peak near 470 cm^{-1} was the bending vibration peak of the Si–O–Si bond. It could be seen from Fig. S2† that the vibration peak of the attapulgite after the pickling step did not change clearly, indicating that the acid treatment process did not destroy the structure of the pristine attapulgite. As presented in Fig. 2, a broad peak at around 3400 cm^{-1} revealed the presence of the isolated silanol groups or of the O–H stretching vibrations of the surface-absorption water molecules. Since the isolated silanol group stretching vibrations were completely shrouded by those of the hydroxyl species in the same location region, it was difficult to distinguish the variation of the isolated silanol groups. Meanwhile, the sharp absorption band centered at around 1080 cm^{-1} originated from the vibration mode of Si–O–Si. The absorption band at 985 cm^{-1} was assigned to the –OH stretching vibration modes of Si–OH. Compared with pristine SBA-15, the peak at 1085 cm^{-1} corresponding to the Si–O bond was shifted to a high wavenumber and narrowed, while the δ_{OH} stretching vibration at 985 cm^{-1} became weaker after the *in situ* doping of aluminum atoms. This phenomenon can be attributed to the substitution of silicon atoms by aluminum atoms and the formation of the Si–Al bond instead of Si–OH groups in Al-SBA-15, verifying the integration of aluminum atoms in the framework. Meanwhile, the Mn/Al-SBA-15 samples exhibited the same IR patterns as Al-SBA-15, illustrating that the basic atomic structure of Al-SBA-15 still remained after the manganese species was loaded.

The N_2 adsorption–desorption isotherms and the pore size distributions of the samples are shown in Fig. 3 and Table 1. All samples in Fig. 3 exhibited adsorption isotherms of type IV with a H1-type hysteresis loop of the nanomaterials with uniform mesopores. It is clear that the adsorption and desorption isotherms show a large increase in the relative pressure (P/P_0) ranging from 0.7–0.8 for Al-SBA-15 and Mn/Al-SBA-15. However, for SBA-15(TEOS), the adsorption and desorption isotherms showed a large increase in the relative pressure (P/P_0) ranging from 0.6–0.8. The different position and increase in the P/P_0 inflection points were directly related to the pore size in the mesopore range, and the sharpness of these steps indicated the uniformity of the pore size. The textual parameters derived from the adsorption–desorption isotherms are listed in Table 1. Table 1 shows that the pore volume and pore diameter grew slightly larger from 0.9760 $cm^3\ g^{-1}$ and 61.8 Å for SBA-15(TEOS) to 1.1070 $cm^3\ g^{-1}$ and 70.5 Å for Al-SBA-15. These increases could be attributed to the doping of Al elements, which was beneficial for the formation of defects in the structure, resulting in the enlargement of the partial mesopores. Moreover, as the MnO_x content increased, the pore volume, pore diameter and specific surface area of Al-SBA-15 decreased markedly, indicating the deposition of MnO_x nanoparticles onto Al-SBA-15.

The morphology and structure of the samples were further characterized by scanning electron microscopy (SEM) and transmission electron microscopy (TEM). Remarkably, Al-SBA-15 in Fig. S3(A and B)† possessed the typical *P6mm* hexagonal morphology with well-ordered 2D arrays, and this was similar to SBA-15(TEOS).[48] It was further demonstrated that Al-SBA-15 with the typical structural characteristics of SBA-15 could be directly prepared from attapulgite. The effects of aluminum doping in the SBA-15 substrate on the distribution of manganese oxide species were investigated, as shown in Fig. 4g–i. In

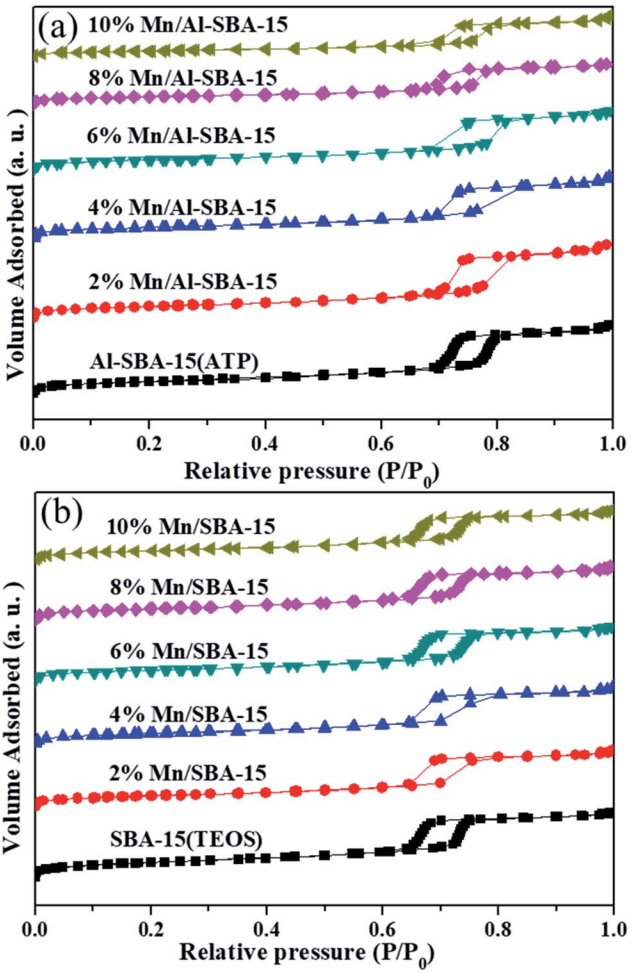

Fig. 3 N_2 adsorption–desorption isotherms of the as-prepared catalysts.

Table 1 The textural parameters of all the catalysts derived from N_2 physisorption results

Catalyst sample	S_{BET} ($m^2\ g^{-1}$)	Average pore size (Å)	Pore volume ($cm^3 \cdot g^{-1}$)
Al-SBA-15(ATP)	563	70.5	1.1070
2% Mn/Al-SBA-15	530	69.8	0.9878
4% Mn/Al-SBA-15	456	67.9	0.9566
6% Mn/Al-SBA-15	387	65.3	0.7902
8% Mn/Al-SBA-15	332	63.2	0.6743
10% Mn/Al-SBA-15	312	58.7	0.6457
SBA-15(TEOS)	614	61.8	0.9760
2% Mn/SBA-15	501	61.4	0.8678
4% Mn/SBA-15	467	61.1	0.8260
6% Mn/SBA-15	435	60.8	0.7825
8% Mn/SBA-15	411	60.8	0.7466
10% Mn/SBA-15	367	60.7	0.7135

This journal is © The Royal Society of Chemistry 2020

Open Access Article. Published on 14 January 2020. Downloaded on 4/16/2026 1:09:03 PM.
This article is licensed under a Creative Commons Attribution-NonCommercial 3.0 Unported Licence.

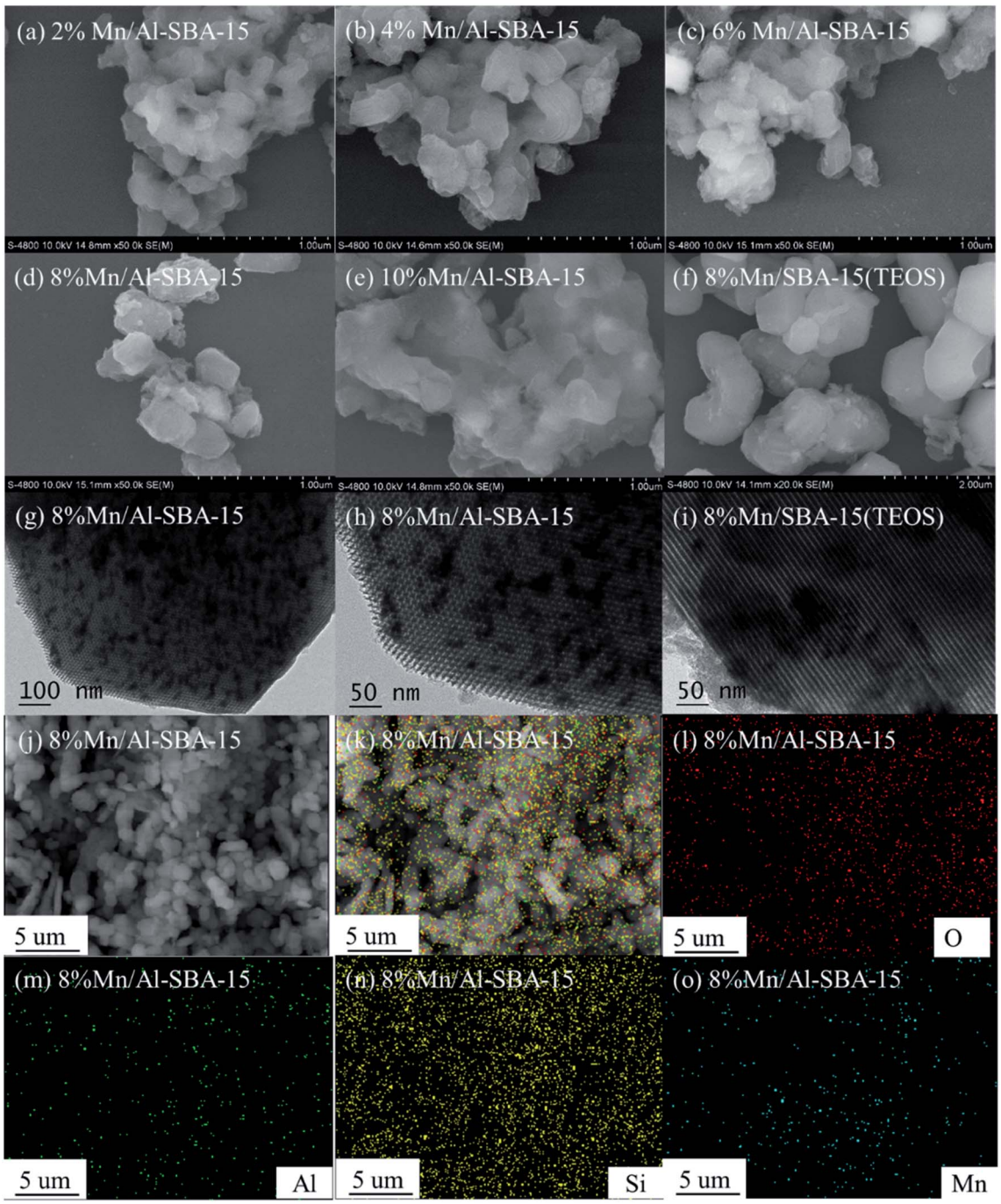

Fig. 4 SEM images and TEM images of the as-prepared catalysts (a–i), and SEM-EDX mapping of 8% Mn/Al-SBA-15 (j–o).

comparison with Mn/SBA-15, manganese oxide nanoparticles were clearly better distributed in the mesoporous pore channels of Al-SBA-15. Meanwhile, the grain size was also much smaller. The occurrence of particle agglomeration on the surface of Mn/SBA-15(TEOS) (Fig. 4i) suggested that Al doping may contribute to the uniform dispersion of smaller MnO_x species and a preferential formation of MnO_x nanoparticles in the channels of SBA-15 (Scheme 2). The X-ray energy dispersive spectroscopy (EDS) elemental mapping in Fig. 4j–o verified the presence of Si, O, Al and Mn elements in the Mn/Al-SBA-15 sample. Noticeably, the distribution of all the elements was homogeneous and uniform, which is consistent with the results of TEM (Fig. 4g) and TEM-EDX (Fig. S4†).

To compare the local structure of Mn/Al-SBA-15 with that of Mn/SBA-15(TEOS), the X-ray absorption fine structure of the Mn-K edge was measured using Mn_2O_3 and MnO_2 as the reference. Fig. 5a exhibits the filtered k3-weighted EXAFS oscillation Fourier transformed into *R* space of the Mn K-edge

Open Access Article. Published on 14 January 2020. Downloaded on 4/16/2026 1:09:03 PM.
This article is licensed under a Creative Commons Attribution-NonCommercial 3.0 Unported Licence.

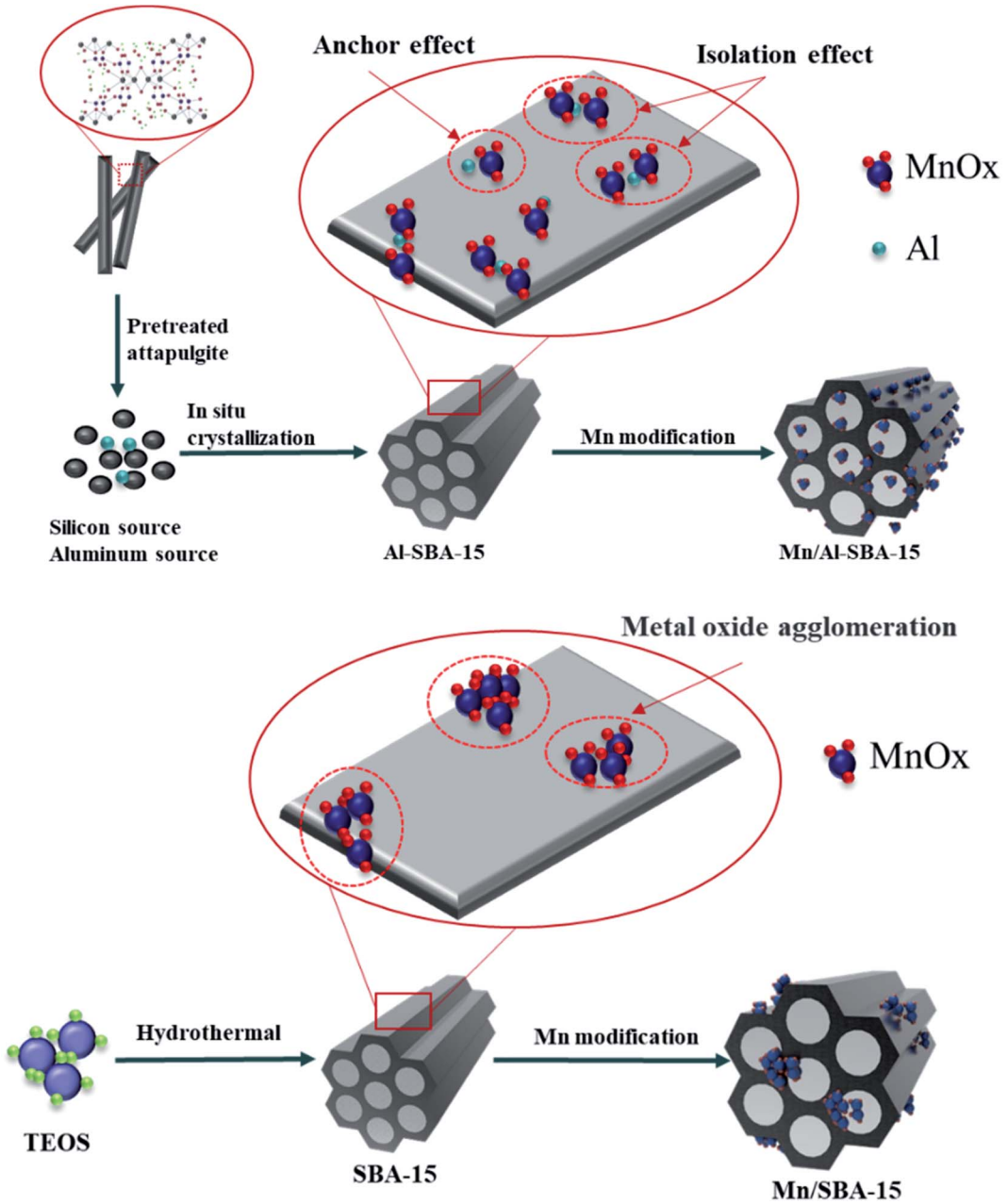

Scheme 2 The synergistic mechanism of Mn modification on Al-SBA-15 and SBA-15.

in 8% Mn/Al-SBA-15 and 8% Mn/SBA-15(TEOS). Both these two catalysts showed similar atomic and electronic structures of Mn with two dominant peaks at around 1.5 Å and 2.5 Å. The peak at around 1.5 Å can be attributed to the closest oxygen (Mn–O) in the MnO_6 octahedra, while the second one at around 2.5 Å can be assigned to the scattering of Mn in the edge-sharing (Mn–Mn edge) MnO_6 octahedra. Based on this analysis, the radial distribution functions (RDFs) of both 8% Mn/Al-SBA-15 and 8% Mn/SBA-15(TEOS) catalysts indicated the coexistence of MnO_2 and Mn_2O_3. According to the bond distance of the standard and reported sample, MnO_2 was identified to be α-MnO_2. Clearly, aluminum doping decreases the coordination number in Mn–Mn, indicating that more abundant crystalline defects are formed involving Mn octahedra that play a key role in the catalytic performance in eliminating VOCs. The normalized Mn K-edge XANES spectra for both 8% Mn/SBA-15(TEOS) and 8% Mn/Al-SBA-15 samples are shown in Fig. 5b. As it has been reported, the edge positions of the manganese oxides shifted to higher energy with the increase in the oxidation state ($MnO < Mn_3O_4 < Mn_2O_3 < MnO_2$).[49] It could easily be found that the edge positions of 8% Mn/SBA-15(TEOS) and 8% Mn/Al-SBA-15 were 6545.2 and 6544.1, and these were located between the positions of MnO_2

 This journal is © The Royal Society of Chemistry 2020

Open Access Article. Published on 14 January 2020. Downloaded on 4/16/2026 1:09:03 PM.
This article is licensed under a Creative Commons Attribution-NonCommercial 3.0 Unported Licence.

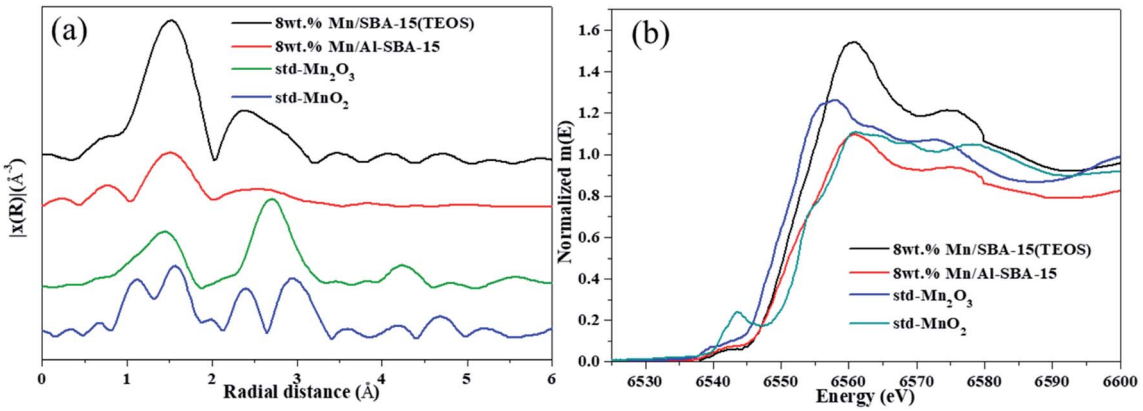

Fig. 5 EXAFS analysis of the Mn K edge (a), and XANES spectra (b) of the as-prepared catalysts.

(6548.3) and Mn_2O_3 (6543.6), indicating the coexistence of Mn^{3+} and Mn^{4+} in both samples.

H_2-TPR measurements were carried out to investigate the redox properties and phase compositions of the catalysts. Fig. 6a presents the TPR profiles of the samples. The broad reduction peaks in the temperature range from 200 to 500 °C were assigned to the reduction of mixed valences of manganese oxide that followed the following reduction pathway: $MnO_2(Mn_2O_3) \rightarrow Mn_3O_4 \rightarrow MnO$.[50] It is worth noting that two peaks could be observed in 8% Mn/SBA-15. The peak at low temperature (319 °C) was assigned to the reduction of MnO_2/Mn_2O_3 to Mn_3O_4, and the other (438 °C) was assigned to the reduction of Mn_3O_4 to MnO. For all the Mn/Al-SBA-15 catalysts, all reduction peaks shifted to lower temperatures considerably in comparison with those of the 8% Mn/SBA-15(TEOS) catalyst, indicating that Al doping into the SBA-15 framework helped to obtain better reducibility. By comparing the reduction behavior of different Mn/Al-SBA-15 samples, corresponding to the results above, 8% Mn/Al-SBA-15 exhibited the lowest reduction temperature (288 °C, 413 °C).

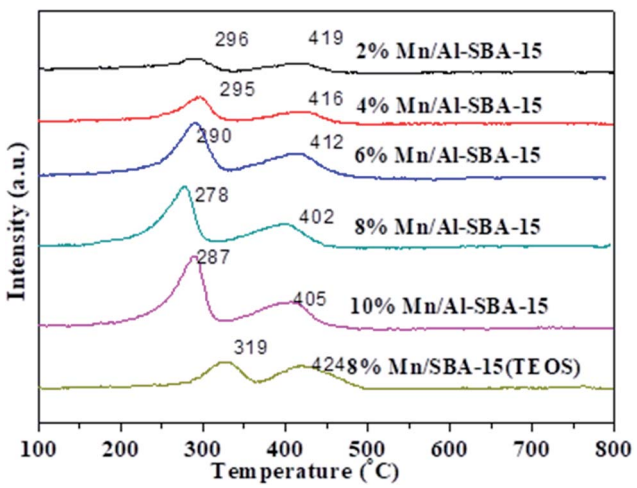

Fig. 6 H_2-TPR profiles of the as-prepared catalysts.

3.2 Catalytic activity and durability

The catalytic activity of Mn/Al-SBA-15 was evaluated under the conditions of toluene concentration = 2000 ppm, and gas hourly space velocity (GHSV) = 60 000 mL $(g\ h)^{-1}$. It can be clearly seen in Fig. 7a that the influence of the Mn loading amount was distinct. Al-SBA-15 exhibited no obvious catalytic activity for toluene oxidation. With the increase of the Mn loading amount, the catalytic oxidation activity of Mn/Al-SBA-15 was significantly enhanced. The sample 8%MnO_x/Al-SBA-15 exhibited the highest toluene conversion, whose T_{50} and T_{90} values were 201 °C and 278 °C, respectively. The excellent catalytic performance of 8% Mn/Al-SBA-15 was mainly attributed to the high content of Mn^{4+}, and not to the larger specific surface area as described above. Additionally, the effect of different GHSV values on the catalytic activity of 8% Mn/Al-SBA-15 was also investigated, as shown in Fig. 7b. Notably, the catalytic activity of the 8% Mn/Al-SBA-15 catalyst highly depended on the GHSV values. As the GHSV increased from 20 000 to 100 000 mL $(g\ h)^{-1}$, the T_{50} and T_{90} values of toluene conversion were elevated by approximately 130 °C at a higher GHSV of 100 000 mL $(g\ h)^{-1}$ (Tables 2 and 3).

In order to examine possible application of the catalysts in real exhaust conditions, the effect of water vapor on the catalytic performance of 8% Mn/Al-SBA-15 was investigated at the GHSV of 60 000 mL $(g\ h)^{-1}$ in the presence of water vapor with different concentrations from 10 vol% to 30 vol%. As shown in Fig. 7c, the toluene conversion remained almost the same after 10 vol%, 20 vol% and 30 vol% of water vapor were respectively introduced at the reaction temperature of 310 °C for at least 8 hours. This observation indicated that water vapor has little inhibition effect in toluene conversion. The 8% Mn/Al-SBA-15 catalyst exhibited excellent catalytic durability in the simulated real exhaust conditions. For a heterogeneous-catalyzed reaction, the durability and recycling of the catalyst played a key role in the practical application. The reaction stability for toluene oxidation over the 8% Mn/Al-SBA-15 catalyst was also investigated and the result is shown in Fig. 7d. The 8% Mn/Al-SBA-15 catalyst exhibited excellent stability in the toluene oxidation reaction for 72 h with the conversion of toluene at over 95%.

Open Access Article. Published on 14 January 2020. Downloaded on 4/16/2026 1:09:03 PM.
This article is licensed under a Creative Commons Attribution-NonCommercial 3.0 Unported Licence.

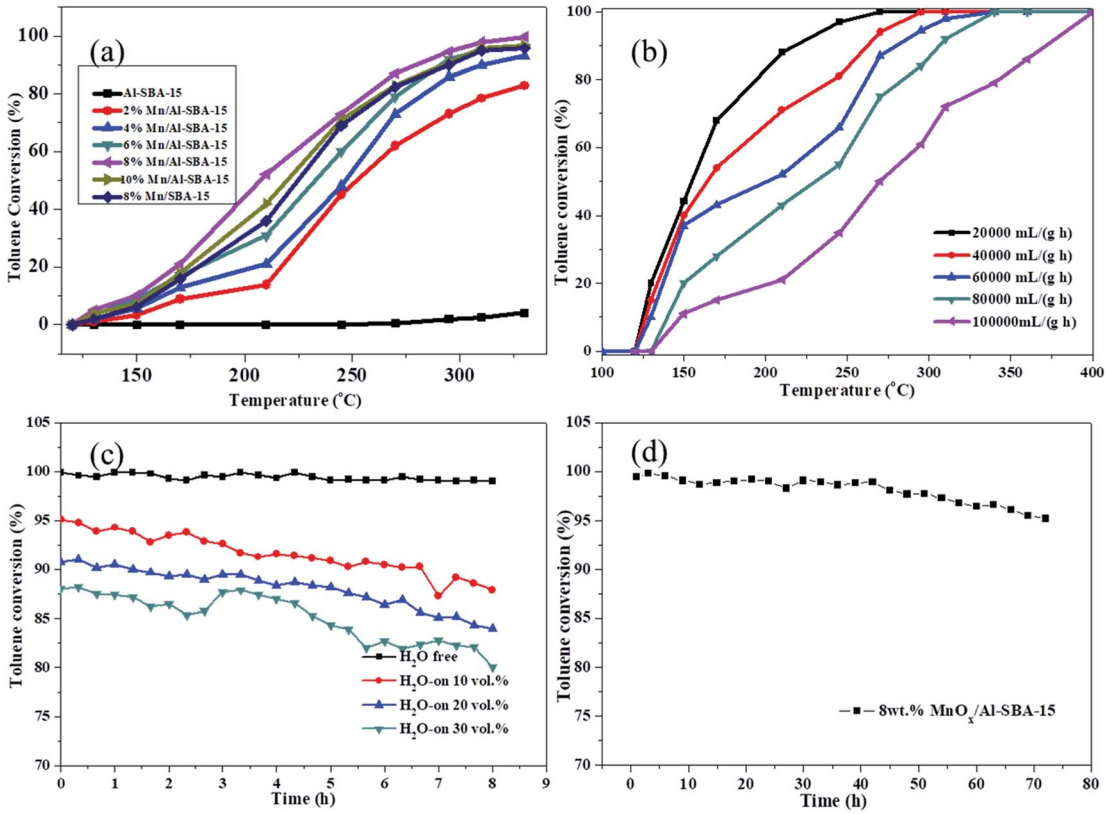

Fig. 7 The catalytic combustion of toluene using different catalysts (a), the effects of GHSV (b) and humidity (c) on the catalytic activity of 8% Mn/Al-SBA-15, and the durability and recycling of the 8% Mn/Al-SBA-15 catalyst (d).

Table 2 The conversion temperatures of toluene over the catalysts

Catalyst	T_{50} (°C)	T_{90} (°C)
2% Mn/Al-SBA-15	252	>350
4% Mn/Al-SBA-15	247	310
6% Mn/Al-SBA-15	218	286
8% Mn/Al-SBA-15	201	278
10% Mn/Al-SBA-15	225	301
8% Mn/SBA-15	223	298

Table 3 The conversion temperatures of toluene over 8% Mn/Al-SBA-15 at different GHSV values

GHSV (mL (g h)$^{-1}$)	T_{50} (°C)	T_{90} (°C)
20 000	155	217
40 000	163	263
60 000	201	278
80 000	230	306
100 000	270	373

4. Conclusions

In summary, a one-pot hydrothermal method combined with an incipient wetness impregnation method was employed to prepare Mn/Al-SBA-15 catalysts from attapulgite and $Mn(NO_3)_2$. Compared to Mn/SBA-15, the as-prepared Mn/Al-SBA-15 catalysts demonstrated significantly enhanced catalytic activity in the catalytic oxidation of toluene. Among them, 8% Mn/Al-SBA-15 exhibited the best performance, with $T_{50} = 201$ °C and $T_{90} = 278$ °C. It also showed excellent water vapor durability and stability during the oxidation of toluene and methyl acetate. Investigations into the structure–activity relationship suggested that both Al doping and manganese loading had great effects on the catalytic combustion performance. Al doping not only enhanced the surface acidity of SBA-15, but also contributed to the uniform dispersion of MnO_x in the pores of Al-SBA-15, accompanied by the active species of manganese that further enhanced the catalytic activity of the catalyst. Manganese loaded on Al-SBA-15 with the high chemical valence of Mn^{4+} plays a key role in the redox properties of the catalysts for the oxidation of toluene. This work presents a systematic investigation into the application of Mn/Al-SBA-15 to the oxidation of toluene, and this might provide a novel approach to exploring more metal oxide/molecular sieve catalysts for the catalytic combustion of VOCs.

Conflicts of interest

The authors declare no competing financial interests.

 This journal is © The Royal Society of Chemistry 2020

Open Access Article. Published on 14 January 2020. Downloaded on 4/16/2026 1:09:03 PM.
This article is licensed under a Creative Commons Attribution-NonCommercial 3.0 Unported Licence.

Acknowledgements

The work was supported by the National Key Research and Development Program of China (2016YFC0204301), the Jiangsu Postdoctoral Foundation (No. 1701014A), the Foundation from State Key Laboratory of Materials-Oriented Chemical Engineering, Nanjing Tech University (ZK201712) and the Postgraduate Research & Practice Innovation Program of Jiangsu Province (KYCX19_0864).

References

1 B. J. Finlayson-Pitts and J. N. Pitts, *Science*, 1997, **276**, 1045–1051.
2 S. Suárez-Vázquez, S. Gil, J. García-Vargas, A. Cruz-López and A. Giroir-Fendler, *Appl. Catal., B*, 2018, **223**, 201–208.
3 G. Zhou, X. He, S. Liu, H. Xie and M. Fu, *J. Ind. Eng. Chem.*, 2015, **21**, 932–941.
4 M. Mao, Y. Li, J. Hou, M. Zeng and X. Zhao, *Appl. Catal., B*, 2015, **174**, 496–503.
5 M. Piumetti, S. Bensaid, T. Andana, N. Russo, R. Pirone and D. Fino, *Appl. Catal., B*, 2017, **205**, 455–468.
6 L. Y. Lin and H. Bai, *Chem. Eng. J.*, 2016, **291**, 94–105.
7 M. Hakim, Y. Y. Broza, O. Barash, N. Peled, M. Phillips, A. Amann and H. Haick, *Chem. Rev.*, 2012, **112**, 5949–5966.
8 M. Zhu, Z. Tong, Z. Zhao, Y. Jiang and Z. Zhao, *Ind. Eng. Chem. Res.*, 2016, **55**, 3765–3774.
9 C. Li, F. Zhang, S. Feng, H. Wu, Z. Zhong and W. Xing, *Ind. Eng. Chem. Res.*, 2018, **57**, 10564–10571.
10 Y. Guo, S. Zhang, J. Zhu, L. Su, X. Xie and Z. Li, *Appl. Surf. Sci.*, 2017, **416**, 358–364.
11 H. J. Joung, J. H. Kim, J. S. Oh, D. W. You, H. O. Park and K. W. Jung, *Appl. Surf. Sci.*, 2014, **290**, 267–273.
12 Y. Wang, S. Xie, J. Deng, S. Deng, H. Wang, H. Yan and H. Dai, *ACS Appl. Mater. Interfaces*, 2014, **6**, 17394–17401.
13 N. Nunotani, N. Moriyama, K. Matsuo and N. Imanaka, *ACS Appl. Mater. Interfaces*, 2017, **9**, 40344–40350.
14 J. Chen, X. Chen, W. Xu, Z. Xu, J. Chen, H. Jia and J. Chen, *Chem. Eng. J.*, 2017, **330**, 281–293.
15 D. M. Gómez, J. M. Gatica, J. C. Hernández-Garrido, G. A. Cifredo, M. Montes, O. Sanz, J. M. Rebled and H. Vidal, *Appl. Catal., B*, 2014, **144**, 425–434.
16 Z. Ye, J. M. Giraudon, N. Nuns, P. Simon, N. De Geyter, R. Morent and J. F. Lamonier, *Appl. Catal., B*, 2018, **223**, 154–166.
17 W. Tang, M. Yao, Y. Deng, X. Li, N. Han, X. Wu and Y. Chen, *Chem. Eng. J.*, 2016, **306**, 709–718.
18 Z. Sihaib, F. Puleo, J. Garcia-Vargas, L. Retailleau, C. Descorme, L. Liotta, J. Valverde, S. Gil and A. Giroir-Fendler, *Appl. Catal., B*, 2017, **209**, 689–700.
19 X. Yang, X. Yu, M. Jing, W. Song, J. Liu and M. Ge, *ACS Appl. Mater. Interfaces*, 2018, **11**, 730–739.
20 B. D. Napruszewska, A. Michalik-Zym, R. Dula, E. Bielańska, W. Rojek, T. Machej, R. P. Socha, L. Lityńska-Dobrzyńska, K. Bahranowski and E. M. Serwicka, *Appl. Catal., B*, 2017, **211**, 46–56.
21 L. Chen, G. Liu, N. Feng, J. Yu, J. Meng, F. Fang, P. Zhao, L. Wang, H. Wan and G. Guan, *Appl. Surf. Sci.*, 2019, **467**, 1088–1103.
22 W. Tang, X. Wu, D. Li, Z. Wang, G. Liu, H. Liu and Y. Chen, *J. Mater. Chem. A*, 2014, **2**, 2544–2554.
23 G. Liu, H. Wang, N. Feng, L. Chen, J. Yu, J. Meng, F. Fang, L. Wang, H. Wan and G. Guan, *Appl. Surf. Sci.*, 2019, **484**, 197–208.
24 Y. Liao, X. Zhang, R. Peng, M. Zhao and D. Ye, *Appl. Surf. Sci.*, 2017, **405**, 20–28.
25 H. Li, G. Lu, Q. Dai, Y. Wang, Y. Guo and Y. Guo, *ACS Appl. Mater. Interfaces*, 2010, **2**, 838–846.
26 T. S. Sreeremya, A. Krishnan, K. C. Remani, K. R. Patil, D. F. Brougham and S. Ghosh, *ACS Appl. Mater. Interfaces*, 2015, **7**, 8545–8555.
27 J. González-Velasco, A. Aranzabal, J. Gutiérrez-Ortiz, R. López-Fonseca and M. Gutiérrez-Ortiz, *Appl. Catal., B*, 1998, **19**, 189–197.
28 X. Zhao, L. Lv, B. Pan, W. Zhang, S. Zhang and Q. Zhang, *Chem. Eng. J.*, 2011, **170**, 381–394.
29 H. Chen, A. Zhong, J. Wu, J. Zhao and H. Yan, *Ind. Eng. Chem. Res.*, 2012, **51**, 14026–14036.
30 A. Corma, *Chem. Rev.*, 1997, **97**, 2373–2420.
31 M. Romero-Sáez, D. Divakar, A. Aranzabal, J. González-Velasco and J. González-Marcos, *Appl. Catal., B*, 2016, **180**, 210–218.
32 J. Gonzalez-Prior, J. I. Gutierrez-Ortiz, R. Lopez-Fonseca, E. Finocchio and B. de Rivas, *Catal. Sci. Technol.*, 2016, **6**, 5618–5630.
33 Y. Dai, V. Pavan Kumar, C. Zhu, M. J. MacLachlan, K. J. Smith and M. O. Wolf, *ACS Appl. Mater. Interfaces*, 2017, **10**, 477–487.
34 Z. Cheng, Z. Chen, J. Li, S. Zuo and P. Yang, *Appl. Surf. Sci.*, 2018, **459**, 32–39.
35 Y. T. Lai, T. C. Chen, Y. K. Lan, B. S. Chen, J. H. You, C. M. Yang, N. C. Lai, J. H. Wu and C. S. Chen, *ACS Catal.*, 2014, **4**, 3824–3836.
36 Z. Qu, X. Zhang, F. Yu, X. Liu and Q. Fu, *J. Catal.*, 2015, **321**, 113–122.
37 H. Yan, W. Chen, G. Liao, X. Li, S. Ma and L. Li, *Sep. Purif. Technol.*, 2016, **159**, 1–6.
38 X. Zhang, H. Dong, Z. Gu, G. Wang, Y. Zuo, Y. Wang and L. Cui, *Chem. Eng. J.*, 2015, **269**, 94–104.
39 W. Zhong, S. R. Kirk, D. Yin, Y. Li, R. Zou, L. Mao and G. Zou, *Chem. Eng. J.*, 2015, **280**, 737–747.
40 J. Xu, W. Wang and A. Wang, *J. Chem. Eng. Data*, 2013, **58**, 764–772.
41 M. Fu, X. Li, R. Jiang and Z. Zhang, *Appl. Surf. Sci.*, 2018, **441**, 239–250.
42 H. Yang, Y. Deng, C. Du and S. Jin, *Appl. Clay Sci.*, 2010, **47**, 351–355.
43 D. Zhao, J. Sun, Q. Li and G. D. Stucky, *Chem. Mater.*, 2000, **12**, 275–279.
44 M. Kruk, M. Jaroniec, C. H. Ko and R. Ryoo, *Chem. Mater.*, 2000, **12**, 1961–1968.
45 Z. Qu, Y. Bu, Y. Qin, Y. Wang and Q. Fu, *Appl. Catal., B*, 2013, **132**, 353–362.

Open Access Article. Published on 14 January 2020. Downloaded on 4/16/2026 1:09:03 PM.
This article is licensed under a Creative Commons Attribution-NonCommercial 3.0 Unported Licence.

46 Z. Qu, D. Chen, Y. Sun and Y. Wang, *Appl. Catal., A*, 2014, **487**, 100–109.
47 Z. Qu, Y. Bu, Y. Qin, Y. Wang and Q. Fu, *Chem. Eng. J.*, 2012, **209**, 163–169.
48 C. Li, Y. Wang, Y. Guo, X. Liu, Y. Guo, Z. Zhang, Y. Wang and G. Lu, *Chem. Mater.*, 2007, **19**, 173–178.
49 Q. Zhang, Y. Wang, S. Itsuki, T. Shishido and K. Takehira, *J. Mol. Catal. A: Chem.*, 2002, **188**, 189–200.
50 H. Chen, Y. Wang and Y. K. Lyu, *Mol. Catal.*, 2018, **454**, 21–29.

 This journal is © The Royal Society of Chemistry 2020